JPE 15-3-17

http://dx.doi.org/10.6113/JPE.2015.15.3.741
ISSN(Print): 1598-2092 / ISSN(Online): 2093-4718

Parallel Operation of Microgrid Inverters Based on Adaptive Sliding-Mode and Wireless Load-Sharing Controls

Qinjin Zhang*, Yancheng Liu†, Chuan Wang*, and Ning Wang*

†*Marine Engineering College, Dalian Maritime University, Dalian, China

Abstract

This study proposes a new solution for the parallel operation of microgrid inverters in terms of circuit topology and control structure. A combined three-phase four-wire inverter composed of three single-phase full-bridge circuits is adopted. Moreover, the control structure is based on adaptive three-order sliding-mode control and wireless load-sharing control. The significant contributions are as follows. 1) Adaptive sliding-mode control performance in inner voltage loop can effectively reject both voltage and load disturbances. 2) Virtual resistive-output-impedance loop is applied in intermediate loop to achieve excellent power-sharing accuracy, and load power can be shared proportionally to the power rating of the inverter when loads are unbalanced or nonlinear. 3) Transient droop terms are added to the conventional power outer loop to improve dynamic response and disturbance rejection performance. Finally, theoretical analysis and test results are presented to validate the effectiveness of the proposed control scheme.

Key words: Adaptive sliding-mode control, Droop control, Microgrid, Power electronic converter, Unbalanced load

I. INTRODUCTION

Microgrid is a low-voltage network with different microsources and distributed loads operating to supply electric power for a local area. Most microsources are interfaced through power electronic converters to provide loads with reliable and high-quality power [1]-[4]. In such systems, every power electric converter should be able to control independently without communication links because of the long distance among microsources [5], [6]. Concurrently, power electric converters should be able to share the variable distributed loads in proportion with the power ratings of converters. To realize the function of power sharing without intercommunication, droop methods that emulate the behavior of large power generators are usually adopted [7]-[11]. The basic prerequisite for applying droop methods is that the equivalent output impedance of the converter should be resistive or inductive. However, in low-voltage microgrids, output impedance is usually resistive-inductive and measuring or estimating is difficult, which makes proportional power sharing impossible [12], [13].

Output impedance is determined through circuit topology, control structure, and line impedance. A possible solution to the impedance problem is adding an inductor in a series with a converter output. However, this inductor is heavy and bulky, and causes imbalance among the three phases. Hence, another method that puts a virtual output impedance loop into the control structure is usually adopted [14], [15]. Given that line impedance is predominantly resistive in low-voltage microgrids, virtual resistive-output-impedance loop is used in this study. Transient droop terms are also added into the conventional droop control method to improve the dynamic response and disturbance rejection performance.

Problems on imbalance and harmonics are also important in the parallel operation of microgrid inverters [16], [17]. The output performance and robustness of microgrid inverters are mainly affected by the effectiveness of the control strategy [18]-[25]. In the past decade, various closed-loop control techniques were reported to achieve the dynamic characteristic and disturbance rejection performance under different types of loads, such as proportional-integral control

Manuscript received Oct. 7, 2014; accepted Jan. 24, 2015
Recommended for publication by Associate Editor Sanjib K. Panda.
†Corresponding Author: liuycdlmu@126.com
Tel: +86-411-84723356, Fax: +86-411-84723356, Dalian Maritime University
*Marine Engineering College, Dalian Maritime University, China

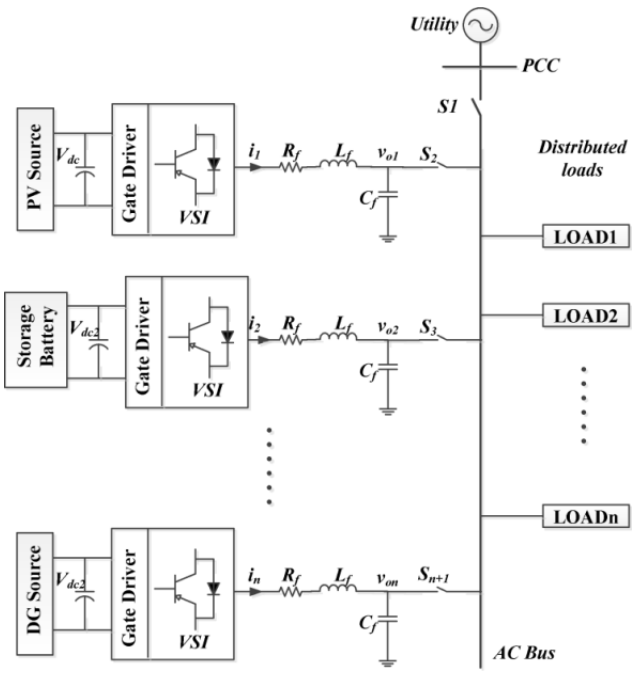

Fig. 1. General microgrid system.

[18], proportional-resonant control [19], [20], Lyapunov-function-based control [21], H∞ control [22], and fuzzy control [23]. However, most of these works are only suitable for three-phase balanced circuit or single-phase circuit, which could also not meet all load conditions, such as unbalanced loads and nonlinear loads. Recently, some works focused on the sliding-mode control method. In [24], a robust sliding-mode controller is proposed to control the active and reactive powers of a doubly fed induction generator wind system without involving any synchronous coordinate transformation. However, the unbalanced condition is not considered in the study. In [25], a combined fuzzy adaptive sliding-mode voltage controller is used for three-phase uninterruptible power supply (UPS) inverter. Moreover, in [26], Mohamed et al. present a direct-voltage control strategy for microgrid converters based on sliding-mode dynamic controller. All these methods can realize robust operation in isolated or grid-connected modes, but output performance is quite poor because of chattering. Hence, this study presents a voltage regulation strategy based on adaptive three-order sliding-mode control. Meanwhile, to solve the unbalanced problem, a combined three-phase four-wire inverter composed of three single-phase full-bridge circuits is adopted.

The remainder of this paper is organized as follows. Section II describes the system which involves the circuit topology and the basic principle of decentralized parallel operation. Section III presents the adaptive three-order sliding-mode voltage control with a virtual resistive-output-impedance loop and wireless load sharing control. Section IV shows the test results, which demonstrate the effectiveness and applicability of the proposed control strategies. Finally, Section V presents the conclusion.

II. System Descriptions

Fig. 1 shows a general microgrid system that consists of distributed generation (DG) units, distributed loads, and voltage source inverters (VSIs) that transfer the energy of DG units into an AC bus. VSIs generally operate in grid-connected mode, and power is transmitted from DG units into the grid. When a fault occurs or the power quality worsens in the utility, the microgrid system disconnects from the grid by cutting off switch S1 and entering intentional islanding mode. DG units and VSIs should be able to share variable distributed loads in proportion with the power ratings of the units and maintain AC bus voltage.

A. Topology and Modeling

Distributed loads are usually unbalanced in actual microgrids, and sometimes single-phase loads are dominant. Hence, in terms of inverter design, the serious load imbalance problem should be considered primarily. The VSI shown in Fig. 2(a) is then adopted for the microgrid power converter in this study, which is composed of three single-phase full-bridge circuits (T1–T12), low-pass filters (L_f and C_f), and an isolated transformer (T). R_f is the per-phase resistance of the *LC* filter, and Z_{line} is the impedance of the line. *u* and *i* are the output voltage and current of the modular inverter circuit respectively, while v_o and i_o are the output voltage and current of the low-pass filter respectively. Subscripts a, b, and c represent the three phases. Each phase in the topology can also be controlled independently.

Before analyzing the VSI model, the following assumptions are made: 1) the isolated transformer T is ideal, and the turn ratio of the transformer is 1:1; 2) all switching devices are ideal, and the delay time can be disregarded. Therefore, the dynamic equation of every phase in the VSI can be represented as follows:

$$\frac{di_{Lf}}{dt} = \frac{1}{L_f}(K_{PWM} v_{con} - v_o - i_{Lf} R_f). \quad (1)$$

$$\frac{dv_o}{dt} = \frac{1}{C_f}(i_{Lf} - i_o), \quad (2)$$

where K_{PWM} is the equivalent parameter of the modular inverter circuit, v_{con} is the input control signal, and $K_{PWM}\ v_{con}$ represents the output voltage of the modular inverter circuit. Eqs. (1) and (2) can be represented as

$$\ddot{v}_o = \frac{R_f}{L_f}\dot{v}_o - \frac{1}{C_f L_f} v_o + \frac{K_{PWM}}{C_f L_f} v_{con} - \frac{1}{C_f}\dot{i}_o - \frac{R_f}{C_f L_f} i_o. \quad (3)$$

Through Laplace transformation, the dynamic model of the single phase shown in Fig. 2(b) can be obtained.

B. Power Sharing Control

Fig. 3 shows the schematic diagram of a microgrid with

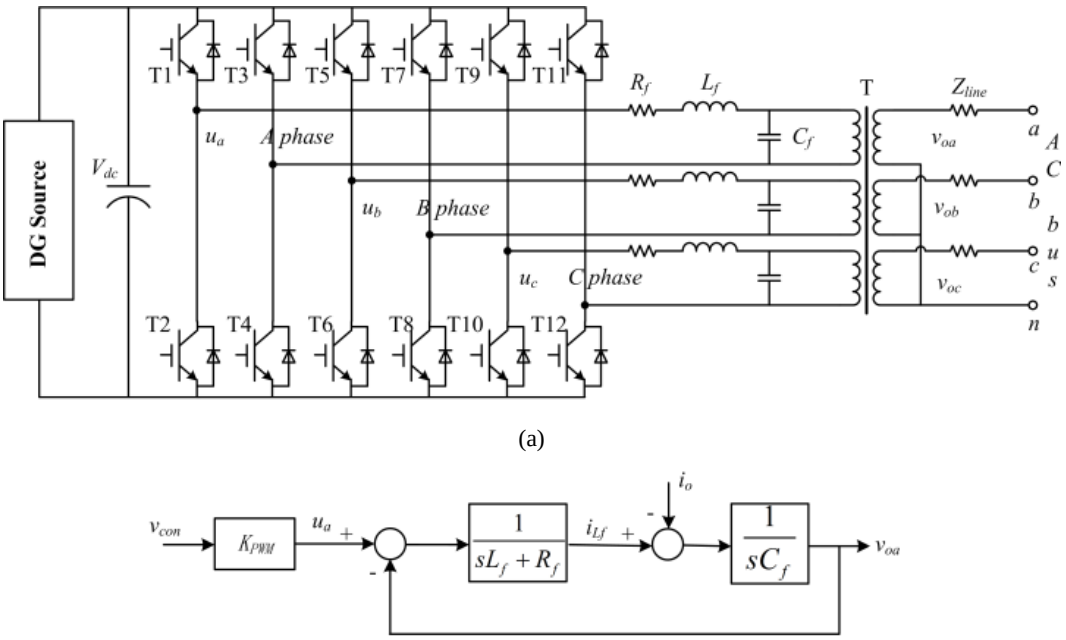

(a)

(b)

Fig. 2. Topology of the inverter and the equivalent dynamic model. (a) Topology of the three-phase four-wire inverter. (b) Equivalent dynamic model of the single phase.

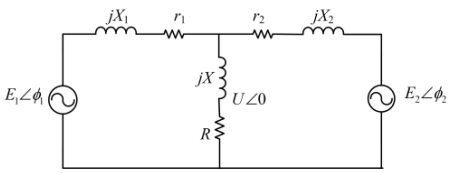

Fig. 3 Equivalent circuit of a microgrid with two inverters.

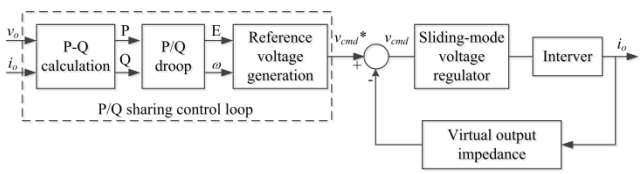

Fig. 4 Proposed control structure of the inverter.

two distributed generations. $U\angle 0$ is the AC bus voltage, and $E_1\angle\phi_1$ and $E_2\angle\phi_2$ are the output voltages of the two inverters. ϕ_i is the phase angle difference between the output and bus voltages. r_i emulates the sum of the output and line resistances, while X_i is the sum of the output and line inductances. The active power and reactive power of inverter *i* can be represented as

$$P_i = \frac{1}{|Z_i|}\left[\left(UE_i\cos\phi_i - U^2\right)\cos\theta_i + UE_i\sin\phi_i\sin\theta_i\right], \tag{4}$$

$$Q_i = \frac{1}{|Z_i|}\left[\left(UE_i\cos\phi_i - U^2\right)\sin\theta_i - UE_i\sin\phi_i\cos\theta_i\right], \tag{5}$$

where $|Z_i|$ is the impedance amplitude of inverter *i*, $|Z_i| = \sqrt{r_i^2 + X_i^2}$, and θ_i is the impedance angle.

Assuming that the impedance of the inverter is resistive ($Z_i = R_i$), the active and reactive powers become

$$P_i = \frac{1}{R_i}\left(UE_i\cos\phi_i - U^2\right), \tag{6}$$

$$Q_i = -\frac{UE_i\sin\phi_i}{R_i}. \tag{7}$$

To realize the power sharing function, conventional droop characteristics are usually used in the parallel operation of microgrid inverters:

$$\begin{cases} E_i = E_i^* + m\left(P_i^* - P_i\right), \\ \omega_i = \omega_i^* - n\left(Q_i^* - Q_i\right) \end{cases} \tag{8}$$

where ω_i^* and E_i^* are the nominal angular frequency and voltage of the inverter respectively. *m* and *n* are the droop coefficients.

C. Output Impedance of the Inverter

Droop control and power-sharing accuracy rely on the impedance angle and amplitude respectively. However, given the existence of line and output impedance differences between the two inverters, the accurate value of the equivalent output impedance is difficult to measure or calculate [14]. In this situation, a method that adds virtual impedance loop into control action is proposed. With a suitably designed virtual impedance, the equivalent output impedance of the inverter can effectively experience either inductive or resistive, and power-sharing accuracy can be greatly improved. In [15], the relationship between equivalent output impedance and power rating of the inverter is derived in detail.

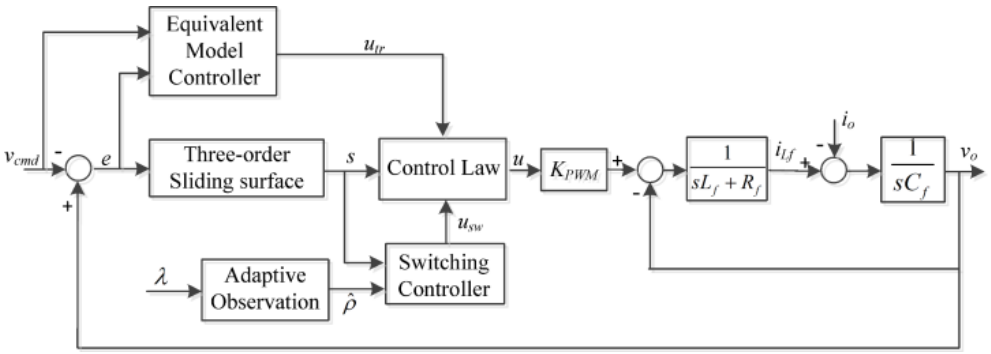

Fig. 5 Block diagram of the output voltage closed loop based on adaptive sliding-mode control

III. CONTROL DESIGN

This section aims to propose a controller that can guarantee parallel operation of microgrid inverters with robust performance and accurate power sharing. The proposed control structure of a microgrid inverter is shown in Fig. 4. The structure consists of three main control loops: 1) inner voltage regulation loop, 2) virtual output impedance loop, and 3) outer P/Q sharing control loop. Given the particularity of the inverter topology adopted in this paper, the inner voltage regulation loop and virtual output impedance loop are controlled independently for each phase, whereas the outer P/Q sharing control loop is calculated for all the phases lumped together.

A. Inner Voltage Regulation Loop

The main objective of the inner voltage regulation loop is to maximize the disturbance rejection performance and have an excellent voltage tracking performance. Based on Eq. (3), the state equation of the single phase can be represented as follows:

$$\ddot{x}(t) = a_p \dot{x}(t) + b_p x(t) + c_p u(t) + n(t), \tag{9}$$

where $x(t) = v_o$, $u(t) = v_{con}$, $a_p = -R_f/L_f$, $b_p = -1/C_f L_f$, $c_p = K_{PWM}/C_f L_f$, and $n(t)$ represents the sum of all uncertainties caused by parameter variation and dynamic and load disturbances. $n(t)$ is assumed to be bounded ($|n(t)|<\rho$).

Define a voltage tracking error $e = v_o - v_{cmd}$ and a three-order dynamic sliding surface $s(t)$ as

$$s(t) = k_1 \int_0^t e(\tau) d\tau + k_2 e(t) + \dot{e}(t), \tag{10}$$

$$\dot{s}(t) = k_1 e(t) + k_2 \dot{e}(t) + \ddot{e}(t), \tag{11}$$

where v_o is the system output voltage, v_{cmd} is the reference voltage command, and k_1 and k_2 are nonzero positive constants.

As shown in Fig. 5, the proposed control scheme in every phase is composed of three parts: equivalent model controller, switching controller, and adaptive observation. The function of the equivalent model controller is to specify the desired performance based on the inverter model, and the output voltage of this controller is u_{tr}. The objective of switching controller is to suppress uncertainties and unpredictable perturbation to ensure the equivalent model controller performance, and the output voltage is u_{sw}. Adaptive observation is designed to alleviate the chattering phenomenon, which is inevitable in the sliding-mode control method. By estimating the upper bound of the uncertainties, the observation can choose the control gain ($\hat{\rho}$) adaptively. According to the dynamic model, the control law can be designed as follows:

$$u = u_{tr} + u_{sw}, \tag{12}$$

$$u_{lb} = -c_p^{-1}\left[k_1 e + k_2 \dot{e} + a_p \dot{v}_o + b_p v_o - \ddot{v}_{cmd}\right], \tag{13}$$

$$u_{sw} = -c_p^{-1} \hat{\rho}(t) \operatorname{sgn}(s(t)), \tag{14}$$

$$\dot{\hat{\rho}}(t) = |s(t)|/\lambda, \tag{15}$$

where λ is a positive constant.

To prove the voltage control law, a Lyapunov function candidate is defined as follows:

$$V(s, \tilde{\rho}) = s^2/2 + \lambda \tilde{\rho}^2/2, \tag{16}$$

where $\tilde{\rho} = \rho - \hat{\rho}$. The derivative of the Lyapunov candidate function is

$$\dot{V}(s(t), \tilde{\rho}(t)) = s(t)\dot{s}(t) + \lambda \tilde{\rho}(t)\dot{\tilde{\rho}}(t). \tag{17}$$

According to Eqs. (12)–(17), the following can be obtained:

$$\begin{aligned} \dot{V}(s(t), \tilde{\rho}(t)) &= s(t)\left[c_p u_{sw} + n(t)\right] + \lambda\left[\rho - \hat{\rho}(t)\right]\dot{\tilde{\rho}}(t) \\ &= s(t)\left[-\hat{\rho}(t)\operatorname{sgn}(s(t)) + n(t)\right] - \\ &\quad \lambda\left[\rho - \hat{\rho}(t)\right]|s(t)|/\lambda \\ &= s(t)n(t) - \rho|s(t)| \\ &\le |s(t)|\left[|n(t)| - \rho\right] \\ &\le 0 \end{aligned} \tag{18}$$

Based on the analysis above, the stable behavior of the adaptive three-order sliding-mode voltage control can be ensured, and the proposed control scheme has no strict requirement for the model parameters. The method of control parameter selection and the analysis of the inverter equivalent output impedance are then described in the following.

By comparing Eqs. (3) and (12), Eq. (19) can be obtained:

$$k_1 e(t) + k_2 \dot{e}(t) + \ddot{e}(t) + \dot{i}_o / C_f + R_f i_o / L_f C_f = -\int_0^t s(\tau) d\tau / \lambda. \tag{19}$$

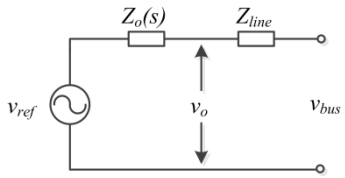

Fig. 6. Equivalent circuit of the inverter with the inner voltage regulation loop.

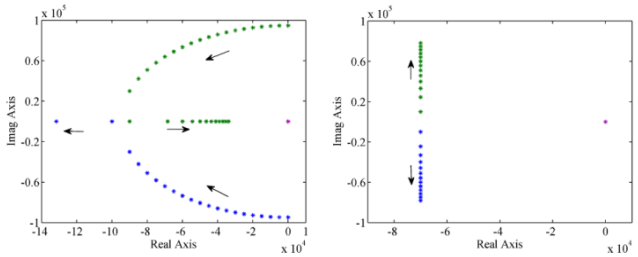

(a) (b)

Fig. 7. Root-locus diagrams. (a) k_1=9×10^9 for 0≤ k_2 ≤2×10^5. (b) k_2=1.4×10^5 for 5×10^9≤ k_1 ≤1×10^{10}.

TABLE I
DETAILS OF THE 3Φ FOUR-WIRE INVERTER

Item	Symbol	Normal value
Filter inductor	L_f	4 mH
Resistance of the inductor	R_f	0.05 Ω
Filter capacitor	C_f	10 μF
Nominal power	S	10 KVA
Nominal voltage	v_o	220 V
Nominal frequency	f_o	50 Hz
Integration constant	k_1	9e9
Proportion constant	k_2	1.4e5
Line impedance	Z_{line}	0.04+j0.005 Ω
P-V droop coefficient	m	3.11e-4 V/W
Q-f droop coefficient	n	2e-4 rad/s/Var

Through Laplace transformation, Eq. (19) can be represented as follows:

$$v_o = v_{cmd} - Z_o(s)\cdot i_o \quad , \qquad (20)$$

$$Z_o(s) = \frac{\lambda}{L_f C_f}\cdot\frac{\left(L_f s + R_f\right)s^3}{\lambda s^5 + \lambda k_2 s^4 + \lambda k_1 s^3 + k_1 s^2 + k_2 s + 1}$$

where $Z_o(s)$ is the output-impedance transfer function. Fig. 6 shows the equivalent circuit of the inverter. Based on Eq. (20), the dynamics of the output voltage is affected by the output impedance of the inverter, and the desired dynamic response can be obtained by adjusting the system poles with the suitable selection of k_1 and k_2. Fig. 7 shows the root locus for different k_1 and k_2 values. Evidently, the poles gradually come close to an imaginary axis as k_2 decreases, hastening the system but making it more oscillatory. In comparison, when k_1 is increased, the poles move farther away from the real axis, resulting in a less damped system.

Table I lists the detailed parameters of the 3φ four-wire inverter. The bode diagram of the output impedance can then be obtained, as shown in Fig. 8. The output impedance value

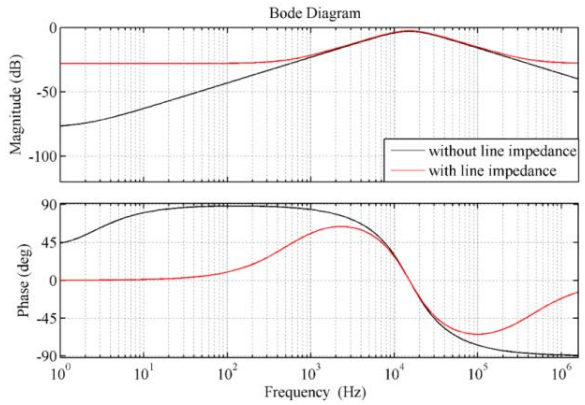

Fig. 8. Bode diagram of the output impedance with and without the line impedance.

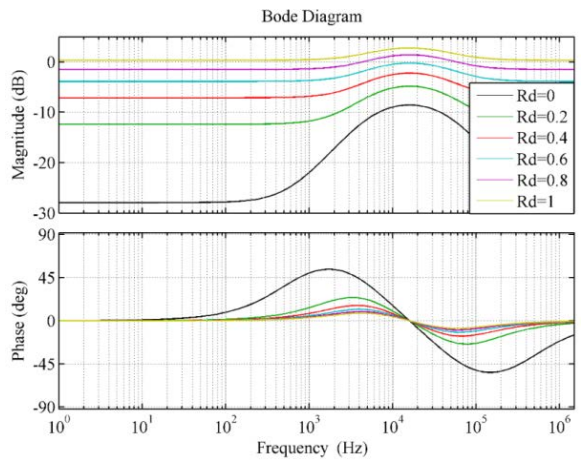

Fig. 9. Bode diagram of the output impedance with *Rd* variation (from 0 to 1).

clearly has comparable resistive and inductive terms at 50, 150, 250, 350 Hz, and so on. For example, at the power frequency (50 Hz), the output impedance is about −50 dB, and 80 deg, whereas if line impedance is considered, the output impedance is about −30 dB and 10 deg.

The phase and amplitude of output impedance is very sensitive to line impedance. Nevertheless, line impedances are difficult to measure and estimate in an actual system; line impedances are usually different among various inverters and even differ among the three phases of an inverter. Thus, power-sharing accuracy among parallel inverters is not guaranteed.

B. Virtual Resistive-Output-Impedance Loop

To meet the requirements of parallel operation for microgrid inverters, virtual output impedance loop is added into the control structure. By dropping the output voltage reference v_{cmd}^* proportionally to the output current, as shown in Fig. 4, the equivalent output impedance of the closed-loop inverter can be changed and fixed. The input reference voltage of the inner loop can then be rewritten as

$$\begin{aligned} v_o &= (v_{cmd}^* - R_d\cdot i_o) - Z_o(s)\cdot i_o \,, \\ &= v_{cmd}^* - Z_o^*(s)\cdot i_o \end{aligned} \qquad (21)$$

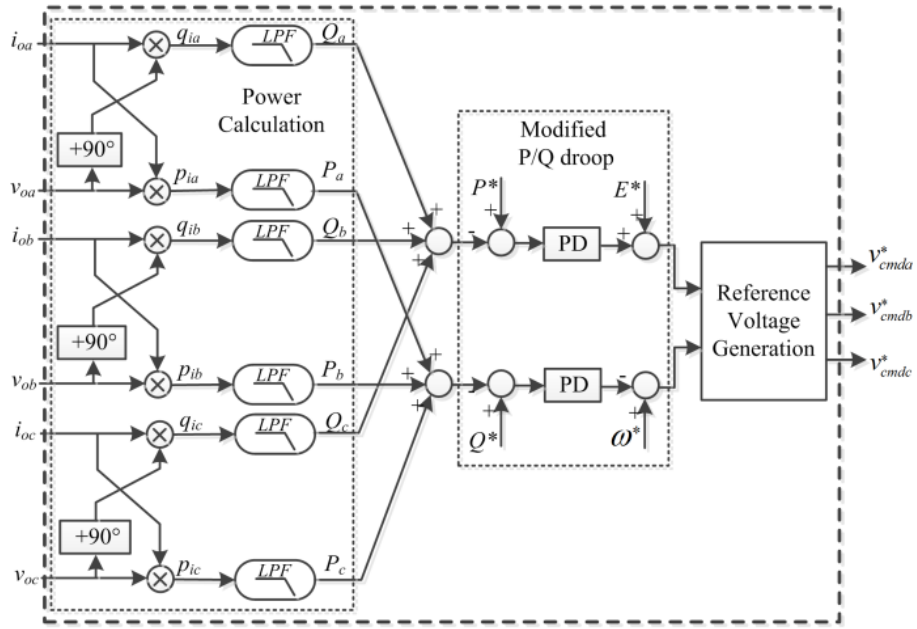

Fig. 10. Block diagram of the power-sharing controller.

where $Z_o^*(s) = R_d + Z_o(s)$ is the new equivalent output impedance of the inverter, and v_{cmd}^* is the voltage reference at no load. Fig. 9 shows the influence of *Rd* on output impedance. Increasing the value of *Rd* leads to increasingly resistive output impedance at the frequencies of 50, 150, 250, 350 Hz, and so on. Concurrently, the magnitudes of the output impedance at such frequencies tend to 20 lg *Rd*. Apparently, as *Rd* increases, the values of the original output and line impedances can be neglected. However, excessive *Rd* value would reduce the voltage reference considerably and cause the steady-state error of the system to increase. Accordingly, through proper design of the *Rd* value, the power-sharing accuracy of the parallel operation for inverters can be ensured, regardless whether the loads are balanced, unbalanced, or nonlinear.

C. Outer P/Q Sharing Control Loop

As shown in Fig. 10, the outer P/Q sharing control loop can be divided into three parts: power calculation, modified P/Q droop, and reference voltage generation. Given the existence of unbalanced loads, the method to calculate the active and reactive powers for each phase is adopted. The instantaneous active and reactive powers can be expressed as follows:

$$p = v_o \cdot i_o, \tag{22}$$

$$q = v_o \cdot H(i_o), \tag{23}$$

where v_o and i_o are the measure values of the output voltage and current for each phase respectively, and $H(i_o)$ demonstrates the Hilbert transform of i_o. Next, *p* and *q* should be processed by low-pass filters (LPFs). Subsequently, the total active and reactive powers are the sum of the three phases. In the figure, subscripts a, b, and c represent the three phases.

In microgrid dynamics, low-frequency oscillation modes generated by power-sharing controllers and power filters are dominant [25]. To enhance the performance of a conventional droop controller, transient droop terms can be added into Eq. (8). Transient droop functions increase the controllability of the power-sharing controller by adding a second degree of freedom in control turning. The modified droop functions are given by

$$E_i = E_i^* + m\left(P_i^* - P_i\right) + m_d \frac{d\left(P_i^* - P_i\right)}{dt}, \tag{24}$$

$$\omega_i = \omega_i^* - n\left(Q_i^* - Q_i\right) - n_d \frac{d\left(Q_i^* - Q_i\right)}{dt}, \tag{25}$$

where m_d and n_d are transient droop coefficients. The proposed control method allows transient response to be modified by acting on the main control parameters while maintaining the static droop characteristics. In addition, the proposed method minimizes the transient circulating current among the modules and further improves the whole system dynamic performance. Coefficients *m* and *n* fix the steady-state control objectives, while m_d and n_d are selected to guarantee stability and excellent transient response.

To investigate the stability and transient response of the system, small-signal analysis is performed [27]. Considering the effect of LPFs, the small-signal dynamics of active and reactive powers [Eqs. (6) and (7)] can be expressed as

$$\hat{P}_i = \frac{\omega_c}{s+\omega_c} \cdot \frac{U}{R_i}\left(\cos\phi_i \cdot \hat{E}_i - E_i \sin\phi_i \cdot \hat{\phi}_i\right), \tag{26}$$

$$\hat{Q}_i = -\frac{\omega_c}{s+\omega_c} \cdot \frac{U}{R_i}\left(\sin\phi_i \cdot \hat{E}_i + E_i \cos\phi_i \cdot \hat{\phi}_i\right), \tag{27}$$

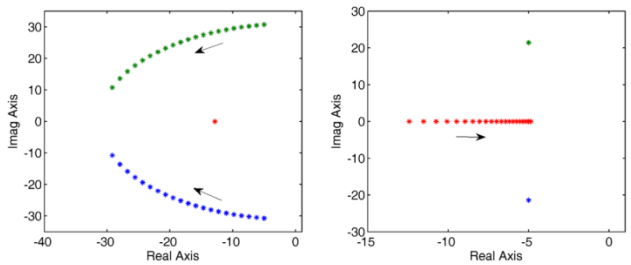

(a) (b)

Fig. 11. Root-locus diagrams. (a) m_d=1×10^{-5} for 0≤ n_d ≤1×10^{-5}. (b) n_d=1×10^{-6} for 0≤ m_d ≤2×10^{-4}.

where $\omega_c/(s+\omega_c)$ is the LPF, ω_c is the cutoff frequency, and $\hat{E}_i$ and $\hat{\phi}_i$ denote the perturbed values of E_i and ϕ_i respectively. By differentiating Eqs. (24) and (25), the following are obtained:

$$\hat{E}_i = -m\hat{P}_i - m_d\dot{\hat{P}}_i, \tag{28}$$

$$\hat{\omega}_i = n\hat{Q}_i + n_d\dot{\hat{Q}}_i. \tag{29}$$

According to Eqs. (26)–(29), the following dynamics can be obtained:

$$\hat{E}_i = -\frac{\omega_c(m+m_d s)}{s+\omega_c}\left(\cos\phi_i\cdot\hat{E}_i - E_i\sin\phi_i\cdot\hat{\phi}_i\right), \tag{30}$$

$$\hat{\phi}_i = -\frac{\omega_c(n+n_d s)}{(s+\omega_c)s}\cdot\frac{U}{R_i}\left(\sin\phi_i\cdot\hat{E}_i + E_i\cos\phi_i\cdot\hat{\phi}_i\right). \tag{31}$$

The characteristic equation of the close-loop system can then be obtained as follows:

$$As^3 + Bs^2 + Cs + D = 0, \tag{32}$$

where

$$A = R_i + m_d\omega_c U\cos\phi_i$$

$$B = \omega_c\left[2R_i + \left(n_d E_i + m + m_d\omega_c\right)U\cos\phi_i + m_d n_d\omega_c E_i U^2/R_i\right]$$

$$C = \omega_c\begin{bmatrix} R_i\omega_c + \left(nE_i + n_d\omega_c E_i + m\omega_c\right)U\cos\phi_i \\ +(mn_d + m_d n)\omega_c E_i U^2/R_i \end{bmatrix}$$

$$D = \omega_c^2 nUE_i\left(\cos\phi_i + mU/R_i\right)$$

According to the characteristics in Eq. (32), system poles can be fixed. System stability and desired dynamical response can then be obtained by adjusting these poles with suitable selection of m_d and n_d. Using the inverter parameters listed in Table I, the root-locus diagrams for different m_d and n_d values are illustrated in Fig. 11. Fig. 11(a) clearly reveals that by decreasing n_d, system poles will be close to an imaginary axis, making the system become oscillatory and even unstable. Fig. 11(b) indicates that by increasing m_d, first-order dynamics will be increasingly dominant, whereas decreasing m_d makes the second-order dynamics become dominant. Hence, transient droop coefficients can be obtained.

IV. Results

This section evaluates the performance of the proposed controller and the parallel operation for the microgrid system depicted in Fig. 1 through simulation and experiment. The test involves two DG units. Both the topologies adopt combined three-phase inverter circuits, as shown in Fig. 2. The circuit and control parameters are presented in Table 2. Fig. 12(a) shows the experimental setup. Only single-phase full-bridge circuits are used in the inverters because of the particularity of the combined three-phase four-wire topology. The design capacities are 5 and 2.5 kW. The composition of INV1 is shown in Fig. 12(b). Depending on the loads, the results of the three cases are discussed in the following sections:

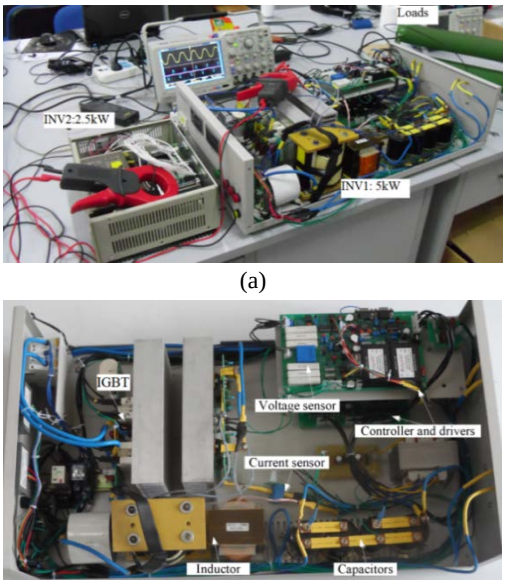

(a)

(b)

Fig. 12. Experimental setup.

TABLE II
Parameters of the Inverters for Parallel Operation

Parameters	Inverter 1	Inverter 2	Units
L_f	4	4	mH
R_f	0.05	0.04	Ω
C_f	10	10	μF
S	10	5	KVA
Z_{line}	0.04+j0.005	0.05+j0.001	Ω
m	3.11e-4	6.22e-4	V/W
n	2e-4	4e-4	rad/s/Var
Rd	0.4	0.8	Ω
ω_c	10	10	rad/s
m_d	5e-5	5e-5	V·s/W
n_d	7e-6	7e-6	rad /Var

A. Case 1: Resistive Load

In this scenario, the simulation and experiment results of sudden load increase and reduction are considered. The initial load of every phase is set as 3 kW, and the load change value is 2 kW.

Figs. 13 and 14 show the simulation results of the parallel

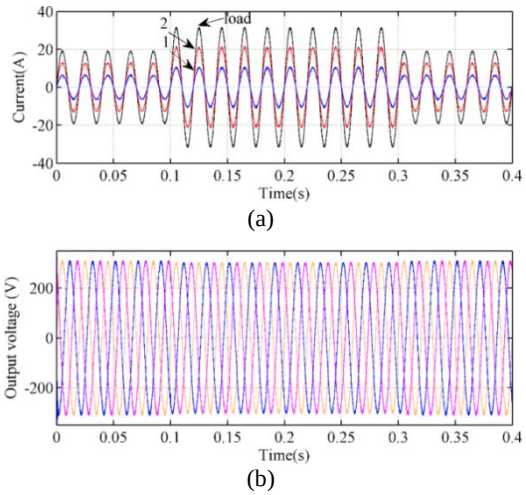

Fig. 13 Simulation results under resistive loads. (a) A-phase currents of the load, INV1 and INV2. (b) Load voltage.

inverters. The commands of sudden load increase and reduction are set in t = 0.1 and 0.3 s respectively. In Fig. 13(a), symbols 1 and 2 represent the output currents of INV1 and INV2 respectively. Obviously, the inverters share the load current proportionately to its power ratings, and the control performance of the transient dynamics is very well that the currents can stabilize in one circle. Fig. 13(b) indicates that output voltage can remain stable when load changes, and the total harmonic distortion (THD) is less than 5%. However, given the existence of virtual resistive-output-impedance loop, very small variations (t = 0.1 and 0.3 s) occur on the output voltage and are almost negligible here. Fig. 14 shows the instantaneous power for load and parallel inverters. P and Q represent the active and reactive powers. Evidently, load power can be shared in proportion with the power rating of the inverter.

The experiment results are shown in Fig. 15. The upper trace is load voltage, and the lower traces are output currents of the two inverters. The output current of INV1 is nearly double of INV2 regardless of whether the inverters operate in steady or transient state. Meanwhile, voltage stability is unaffected by the transient state.

The simulation and experiment results show that the proposed control structure is effective for parallel inverters under resistive loading condition, and power-sharing accuracy and dynamic response can be ensured.

B. Case 2: Resistive-Inductive Load

Resistive-inductive loading condition with a sudden change is considered in this scenario.

The simulation results are shown in Figs. 16 and 17. The initial loads of every phase are set as P = 3 kW, Q = 1 kVar, and the load change values are P = 1 kW, Q = 2 kVar. The variation commands of the loads are set in t = 0.1 and 0.3 s. Fig. 16 shows the output voltage and current responses of the two inverters. The output currents of INV1 and INV2 are

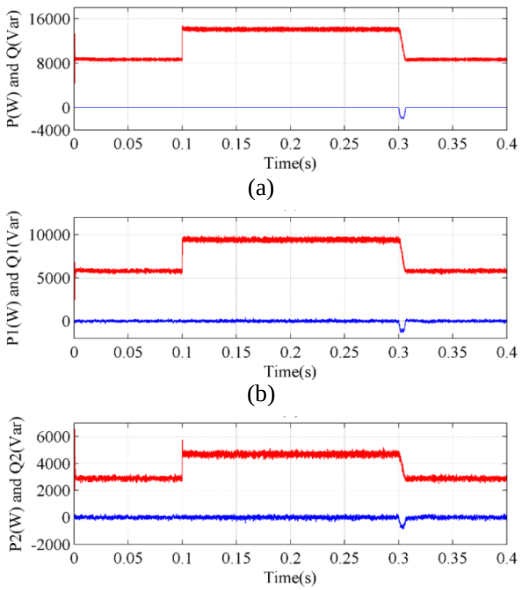

Fig. 14. Simulation results under resistive loads. (a) Active power (upper trace) and reactive power (lower traces) responses of the loads. (b) Power responses of INV1. (c) Power responses of INV2.

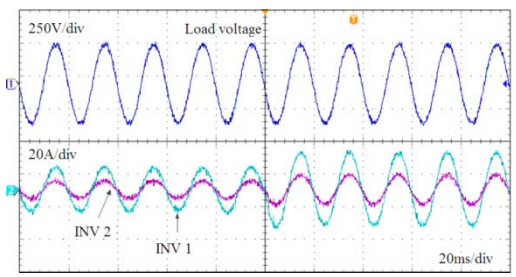

Fig. 15. Experiment results under resistive loads: load voltage (upper trace) and output currents (lower traces) of INV1 and INV2.

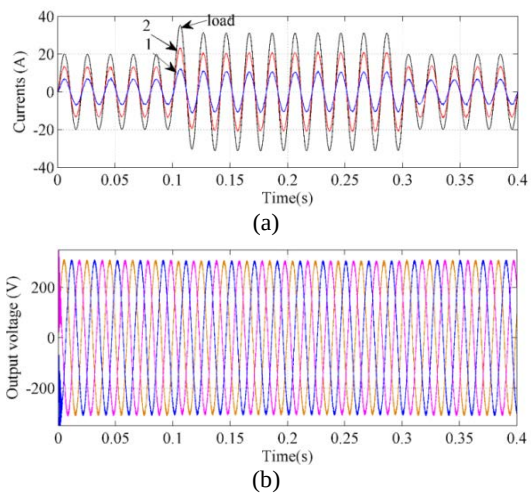

Fig. 16. Simulation results under resistive-inductive loads. (a) A-phase currents of loads INV1 and INV2. (b) Load voltage.

proportional to the power rating of both inverters, and resistive-inductive load cannot affect the power-sharing

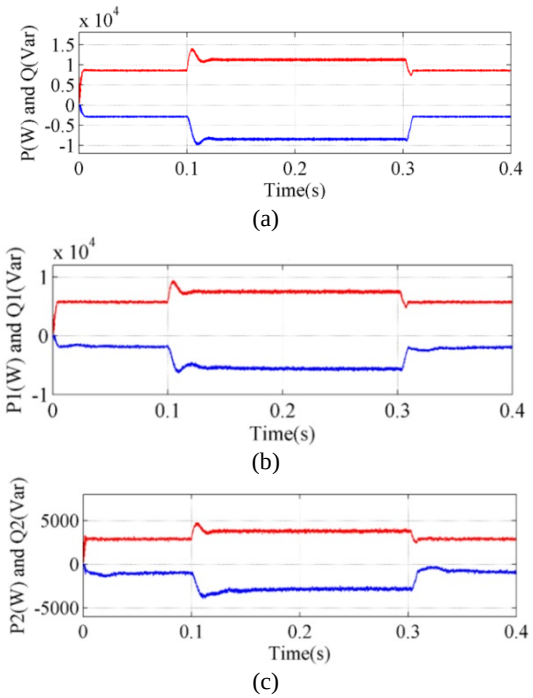

Fig. 17. Simulation results under resistive-inductive loads. (a) Active power (upper trace) and reactive power (lower traces) responses of the loads. (b) Power responses of INV1. (c) Power responses of INV2.

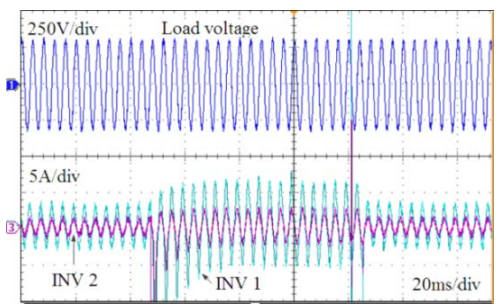

Fig. 18. Experiment results under resistive-inductive loads: load voltage (upper trace) and output currents (lower traces) of INV1 and INV2

accuracy and stability of the output voltage. Meanwhile, the current dynamics can stabilize within two circles. Fig. 17 shows the performance of the instantaneous power. Compared with the resistive loading condition, the transient response is longer.

To test the robustness of the proposed control structure, pure inductive loads are added to the system in the experiment, as shown by the results in Fig. 18. The transient voltage disturbances are effectively rejected because of the robust sliding-mode control performance. Furthermore, the power sharing accuracy between the two inverters is ensured.

C. Case 3: Unbalanced and Nonlinear Loads

Unbalanced and nonlinear loading conditions are considered in this scenario.

To test the robustness of the proposed control strategies in

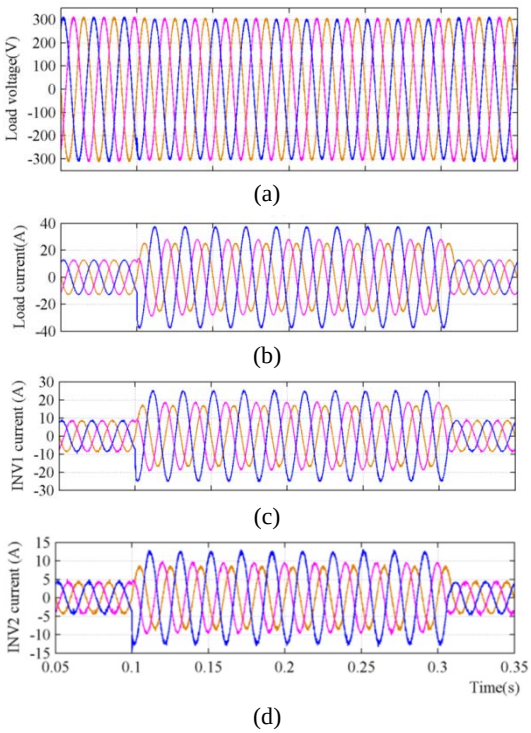

Fig. 19. Simulation results under unbalanced loads. (a) Load voltage. (b) Load current. (c) INV1 output current; and (d) INV2 output current.

rejecting unbalanced disturbances, unbalanced loads are added into the system in the time period 0.1 s < t < 0.3 s. The simulation performance of the load voltage and current under unbalanced loads are shown in Figs. 19(a) and 19(b). The three phase current amplitudes and phases differ, but the load voltage remains balanced. The three-phase voltages are balanced because of the special topology used in this study. The output current waveforms of INVs are shown in Figs. 19(c) and 19(d). The current amplitudes of INV1 and INV2 are proportional to the power ratings of both inverters. The current phases of INV1 and INV2 are also the same; thus, power-sharing accuracy under unbalanced loading condition is ensured.

To test the robustness of the proposed control strategies under nonlinear loading condition, the uncontrolled rectifier circuit is used, and load power is set to 10 kW. The simulation results are shown in Fig. 20. Fig. 20(a) shows the load voltage waveform, and the frequency spectra of this waveform are analyzed in Fig. 20(c). The output voltage, which yields a THD of 1.21%, is regulated to reject nonlinear load disturbances. The load and output currents of the INVs are shown in Fig. 20(b). The frequency spectra are correspondingly analyzed in Figs. 20(d)–20(f). The THDs of these currents (35%, 34.95%, and 35.19%) are nearly the same.

In the experiment, the load power of the single-phase uncontrolled rectifier circuit is set to 1 kW; the results are shown in Fig. 21. Compared with the simulation results, the

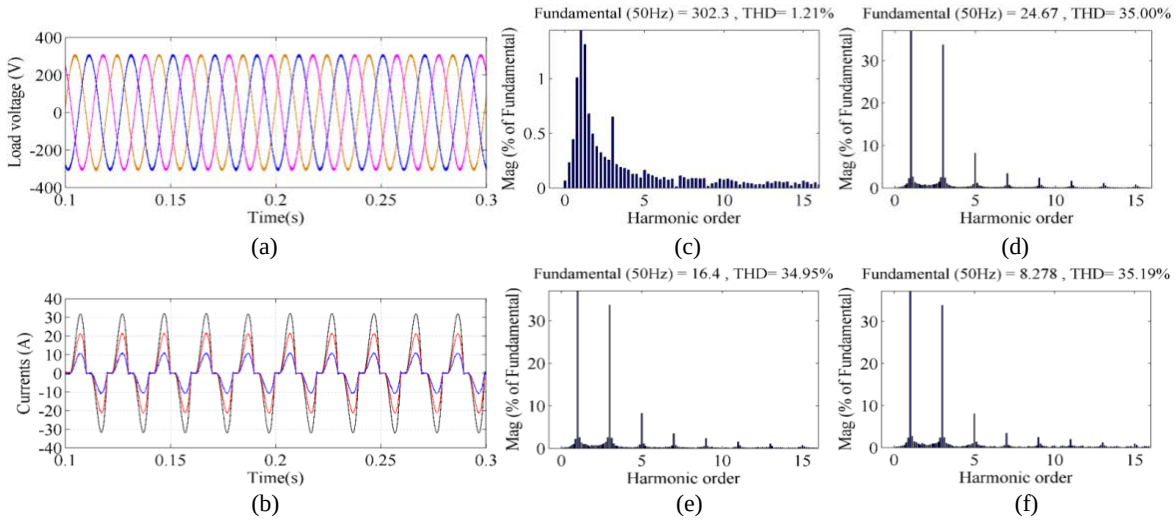

Fig. 20. Simulation results under nonlinear loads. (a) Load voltage. (b) A-phase currents of the load, INV1 and INV2. (c) Load voltage spectra. (d) Load current spectra. (e) Output current spectra of INV1. (f) Output current spectra of INV2.

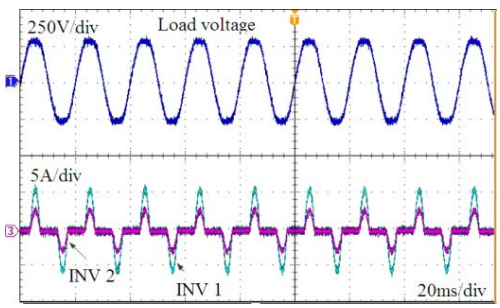

Fig. 21. Experiment results under nonlinear loads: load voltage (upper trace) and output currents (lower trace) of INV1 and INV2.

load voltage and output currents have higher THDs. However, the power-sharing accuracy is maintained. The inverters share not only the fundamental currents, but also the harmonic currents. Thus, power-sharing accuracy under nonlinear loading condition is ensured.

The aforementioned results show that the proposed adaptive sliding-mode control and dynamic load sharing control can be used effectively and reliably under different loading conditions for the parallel operation of microgrid inverters.

V. Conclusion

A new solution for the parallel operation of microgrid inverters in terms of circuit topology and control structure is proposed in this study. The three-phase four-wire inverter composed of three single-phase full-bridge circuits is adopted. The control structure consists of three nested loops: 1) inner voltage regulation loop, 2) virtual output impedance loop, and 3) outer P/Q sharing control loop. Adaptive sliding-mode control is used in the inner voltage loop for the output voltage of the inverter to effectively reject load disturbances, regardless whether loads are balanced, unbalanced, or nonlinear. In a precise contrast with the conventional droop method and the actual low-voltage microgrid, virtual resistive-output-impedance loop is used to enforce the equivalent output impedance of the inverters to be resistive and proportional. Finally, a new wireless power-sharing control method that involves transient droop terms is adopted in the outer P/Q sharing loop. Consequently, excellent power-sharing accuracy can be achieved for all kinds of loads: balanced, unbalanced, or nonlinear. Meanwhile, system stability and dynamic response can also be improved. Finally, theoretical analysis and test results verify the effectiveness and superiority of the proposed control structure.

Acknowledgment

This work was supported by the National Nature Science Foundation of China under Grant 51479018, and by the Fundamental Research Funds for the Central Universities under Grant 3132014322.

References

[1] R. H. Lasseter, J. H. Eto, B. Schenkman, J. Stevens, H. Vollkommer, D. Klapp, E. Linton, H. Hurtado, and J. Roy, "CERTS microgrid laboratory test bed," *IEEE Trans. Power Del.*, Vol. 26, No. 1, pp. 325-332, Jan. 2011.

[2] X. Wang, J. M. Guerrero, F. Blaabjerg, and Z. Chen, "A review of power electronics based microgrids," *Journal of Power Electronics*, Vol. 12, No. 1, pp. 181-192, Jan. 2012.

[3] B. Zhao, X. S. Zhang, and J. Chen, "Integrated microgrid laboratory system," *IEEE Trans. Power Syst.*, Vol. 27, No. 4, pp. 2175-2185, Nov. 2012.

[4] J. Rocabert, A. Luna, F. Blaabjerg, and P. rodriguez, "Control of power converters in AC microgrids," *IEEE Trans. Power Electron.*, Vol. 27, No. 11, pp. 4734-4749, Nov. 2012.

[5] E. A. A. Coelho, P. C. Cortizo, and P. F. D. Garcia, "Small-signal stability for parallel-connected inverters in stand-alone AC supply systems," *IEEE Trans. Ind. App.*, Vol. 38, No. 1, pp. 533-542, Mar. 2002.
[6] P. H. Divshali, A. Alimardani, S. H. Hosseinian, and M. Abedi, "Decentralized cooperative control strategy of microsources for stabilizing autonomous VSC-based microgrids," *IEEE Trans. Power Syst.*, Vol. 27, No. 4, pp. 1949-1959, Nov. 2012.
[7] T. L. Vandoorn, B. Meersman, J. D. M. D. Kooning, and L. Vandevelde, "Directly-coupled synchronous generators with converter behavior in islanded microgrids," *IEEE Trans. Power Syst.*, Vol. 27, No. 3, pp. 1395-1406, Aug. 2012.
[8] H. Bevrani, T. Ise, and Y. Miura, "Virtual synchronous generators: a survey and new perspectives," *International Journal of Electrical Power and Energy Systems*, Vol. 54, pp. 244-254, 2014.
[9] Y. Mohamed and E. F. El-Saadany, "Adaptive decentralized droop controller to preserve power sharing stability of paralleled inverters in distributed generation microgrids," *IEEE Trans. Power Electron.*, Vol. 23, No. 6, pp. 2806-2816, Nov. 2008.
[10] C. Cho, J. H. Jeon, J. Y. Kim, S. Kwon, K. Park, and S. Kim, "Active synchronizing control of a microgrid, " *IEEE Trans. Power Electron.*, Vol. 26, No. 12, pp. 3707-3719, Dec. 2011.
[11] C. N. Rowe, T. J. Summers, R. E. Betz, and D. J. Comforth, and T. G. Moore, "Arctan power–frequency droop for improved microgrid stability," *IEEE Trans. Power Electron.*, Vol. 28, No. 8, pp. 3747-3759, Aug. 2013.
[12] J. M. Guerrero, L. G. Vicuña, J. Matas, M. Castilla, and J. Miret, "Output impedance design of parallel-connected UPS inverters with wireless load-sharing control, " *IEEE Trans. Ind. Electron.*, Vol. 52, No. 4, pp. 1126-1135, Aug. 2005.
[13] J. Kim, J. M. Guerrero, P. Rodriguez, R. Teodorescu, and K. Nam, "Mode adaptive droop control with virtual output impedances for an inverter-based flexible AC microgrid," *IEEE Trans. Power Electron.*, Vol. 26, No. 3, pp. 689-701, Mar. 2011.
[14] D. De and V. Ramanarayanan, "Decentralized parallel operation of inverters sharing unbalanced and nonlinear loads," *IEEE Trans. Power Electron.*, Vol. 25, No. 12, pp. 3015-3025, Dec. 2010.
[15] J. M. Guerrero, J. Matas, L. G. Vicuna, M. Castilla, and J. Miret, "Decentralized control for parallel operation of distributed generation inverters using resistive output impedance," *IEEE Trans. Ind. Electron.*, Vol. 54, No. 2, pp. 994-1004, Apr. 2007.
[16] D. De and V. Ramanarayanan, "A proportional + multiresonant controller for three-Phase four-wire high-frequency link inverter," *IEEE Trans. Power Electron.*, Vol. 25, No. 4, pp. 899-906, Apr, 2010.
[17] M. B. Delghavi and A. Yazdani, "Islanded-mode control of electronically coupled distributed-resource units under unbalanced and nonlinear load conditions," *IEEE Trans. Power Del.*, Vol. 26, No. 2, pp. 661-673, Apr. 2011.
[18] Z. Guo, D. Sha, and X. Liao, "Wireless paralleled control strategy of three-phase inverter modules for islanding distributed generation systems," *Journal of Power Electronics*, Vol. 13, No. 3, pp. 479-486, May 2013.
[19] S. Mehdi, J. Alireza, C. V. Juan, and J. M. Guerrero, "Autonomous voltage unbalance compensation in an islanded droop-controlled microgrid," *IEEE Trans. Ind. Electron.*, Vol. 60, No. 4, pp. 1390-1402, Apr. 2013.
[20] A. Hasanzadeh, O. C. Onar, H. Mokhtari, and A. Khaligh, "A proportional-resonant controller-based wireless control strategy with a reduced number of sensors for parallel-operated UPSs," *IEEE Trans. Power Del.*, Vol. 25, No. 1, pp. 468-478, Jan. 2010.
[21] S. Dasgupta, S. N. Mohan, S. K. Sahoo, and S. K. Panda, "Lyapunov function-based current controller to control active and reactive power flow from a renewable energy source to a generalized three-phase microgrid system," *IEEE Trans. Ind. Electron.*, Vol. 60, No. 2, pp. 799-813, Feb. 2013.
[22] T. Hornik, and Q. C. Zhong, "Parallel PI voltage–H∞ current controller for the neutral point of a three-phase inverter," *IEEE Trans. Ind. Electron.*, Vol. 60, No. 4, pp. 1335-1343, Apr. 2013.
[23] N. Altin, and I. Sefa, "dSPACE based adaptive neuro-fuzzy controller of grid interactive inverter," *Energy Convention and Management*, Vol. 56, pp. 130-139, Apr. 2012.
[24] R. Aghatehrani, and R. Kavasseri, "Sensitivity-analysis -based sliding mode control for voltage regulation in microgrids," *IEEE Trans. Sustain. Enerergy*, Vol. 4, No. 1, pp. 50-57, Jan. 2013.
[25] K. Naheem, Y.-S. Choi, F. Mwasilu, H. H. Choi, and J.-W. Jung, "Design and stability analysis of a fuzzy adaptive SMC system for three-phase UPS inverter," *Journal of Power Electronics*, Vol. 14, No. 4, pp. 704-711, Jul. 2011.
[26] Y. A. I. Mohamed, H.H. Zeineldin, M. M. A. Salama, and R. Seethapathy, "Seamless formation and robust control of distributed generation microgrids via direct voltage control and optimized dynamic power sharing," *IEEE Trans. Power Electron.*, Vol.27, No. 3, pp. 1283-1294, Mar. 2012.
[27] R. Majumder, "Some aspects of stability in microgrids," *IEEE Trans. Power Syst.*, Vol. 28, No.3, pp. 3243-3252, Aug. 2013.

Qinjin Zhang was born in Jiangsu, China in 1986. He received his B.S. and M.S. degrees in Electrical Engineering from Dalian Maritime University, Dalian, China in 2009 and 2011 respectively. He is currently pursuing his Ph.D. in Marine Engineering from Dalian Maritime University, Dalian, China. His current research interests include distributed power generation technology, power electronics converters, and microgrids.

Yancheng Liu was born in Liaoning, China. He received his B.S. and M.S. degrees in Electrical Engineering from Harbin Industrial University, Harbin, China, and his Ph.D. degree in Marine Engineering from Dalian Maritime University, Dalian, China in 1985, 1988, and 2002, respectively. He is currently a professor in the Marine Engineering College at Dalian Maritime University, Dalian, China. His current research interests include AC motor control, power electronic converters, ship electrical propulsion technology, renewable energy systems, and microgrids.

Chuan Wang was born in Liaoning, China in 1985. He received his M.S., B.S., and Ph.D. degrees from the Marine Engineering College, Dalian Maritime University, Dalian, China in 2007, 2009, and 2012, respectively. He is currently a lecturer in the Marine Engineering College in Dalian Maritime University, Dalian, China. His current research interests include power systems, intelligence artificial algorithms, particle swarm optimization, and system identification.

Ning Wang was born in Shandong, China in 1983. He received his B.Eng. degree in Marine Engineering and Ph.D. degree in Control Theory and Engineering from Dalian Maritime University, Dalian, China in 2004 and 2009 respectively. From September 2008 to September 2009, he was financially supported by the China Scholarship Council to work as a joint-training Ph.D. student at the Nanyang Technological University, Singapore. He is currently an Associate Professor in the Marine Engineering College in Dalian Maritime University, Dalian, China. His research interests include AC motor control, robust control theory, artificial neural networks, fuzzy systems, machine learning, and ship intelligent control.